Soils surrounding saline-alkaline lakes of Nhecolândia, Pantanal, Brazil: Toposequences, mineralogy and chemistry

André Renan Costa-Silva, Yves Lucas, Ary Tavares Rezende-Filho, Mariana Dias Ramos, Patricia Merdy, Débora Ayumi Ishida, Laurent Barbiero, Adolpho José Melfi, Célia Regina Montes

Soils surrounding saline-alkaline lakes of Nhecolândia, Pantanal, Brazil: toposequences, mineralogy and chemistry.

André Renan Costa-Silva[1,*], Yves Lucas[2], Ary Tavares Rezende Filho[3], Mariana Dias Ramos[4], Patricia Merdy[2], Débora Ayumi Ishida[5], Laurent Barbiero[6], Adolpho José Melfi[5], Célia Regina Montes[1, 5]

[1]CENA, LEST, Universidade de São Paulo, Piracicaba 13400-970, Brasil.

[2]Université de Toulon, Aix Marseille Univ, CNRS, IM2NP, 83041 Toulon CEDEX 9, France.

[3]FAENG, Universidade Federal do Mato Grosso do Sul, Campo Grande 79079-000, Brasil

[4]IGCE, Universidade Estadual Paulista, Rio Claro 13506-900, Brasil

[5]IEE, LEST, Universidade de São Paulo, São Paulo 05508-010, Brasil.

[6]GET, IRD, CNRS, UPS, OMP, Toulouse 31400, France

*Corresponding author.

Abbreviations: DOC: Dissolved organic carbon; DOM: Dissolved organic matter; EC_S: Soil apparent electrical conductivity; EC_W: Water electrical conductivity; EG: Ethylene glycol; ODFE: Oven-dried fine earth; OMF: Organic matter free.

E-mail address: andrerenan00@usp.br (A. R. Costa-Silva).

Postal address: Centro de Energia Nuclear na Agricultura (CENA), Universidade de São Paulo, Av. Centenário, 303, São Dimas, 13416-000, Piracicaba, São Paulo, Brasil.

Contact numbers: +5585981828161 or +330615278748

ABSTRACT

The Nhecolândia subregion of the Brazilian Pantanal is a vast fluviolacustrine system subject to a very seasonal climate, which is distinguished by freshwater or saline-alkaline lakes of different types: green due to cyanobacterial bloom, black due to dissolved organic matter, or crystalline. Numerous studies carried out in the region over the past twenty years on the lakes and the surrounding soils have shown probable relationships between the saline-alkaline character of the lakes, the surrounding soils and the dynamics of the water tables. These results, however, have been acquired by independent studies on many different sites, which makes their synthesis difficult, and they leave

open the question of the causes of the difference between lake types. Here we have begun to study on a single site representative of the Nhecolândia area, all the factors thought to be necessary to understand the genesis and dynamics of the soils and lakes. For each type of lake, we carried out detailed toposequence soil studies and characterized the granulometry, chemistry and mineralogy of the identified horizons. A 45-month temporal study of satellite data was used to assess the connection of the lakes to the seasonal flood network. Our results confirmed the general organization and mineralogy of the soil covers around saline-alkaline lakes. We have determined the differences between the soil toposequences corresponding to the slopes of the different types of lakes. We have found that two types of silcrete can be formed, one being acidic and the other alkaline. We have shown that, among the conditions which guarantee endorheism, which leads to the alkalinization of lakes, the presence of a ridge around a lake is not sufficient, but that the presence of deep impermeable horizons in the lower half of the toposequences is necessary. Crystalline lakes could differentiate from black and green ones due to less efficient hydraulic isolation. We

provide a large data set relative to a single site which will help guide and develop more specific studies on these alkaline systems.

Keywords: Pantanal, Nhecolândia, Arenosols, Solonetz, Silcrete, Petroduric horizon.

1. INTRODUCTION

The Pantanal subregion of Nhecolândia is a large lacustrine system developed on sandy sediments deposited from the Pleistocene to the Upper Holocene. The lakes are formed by the partial obstruction of river beds by small forested ridges, locally known as *cordilheiras*, in the distal portion of distributary lobes of the Taquari river sedimentary megafan (Assine et al., 2015). With more than 10,000 lakes, which are mostly shallow and ranging from 0.025 to 0.15 km² (Costa et al., 2015; Pereira et al., 2020). The lacustrine system is dominated by freshwater lakes, knows locally as *baías*, but around 7% are saline-alkaline lakes or *salinas*, surrounded by alkaline soils (Almeida, 2007; Furian et al., 2013). Saline-alkaline lakes can still be subdivided according to the color of their waters which varies between green, due to the proliferation of cyanobacteria, black, due to high

concentrations of dissolved organic matter (DOM) and crystalline (Barbiero et al., 2008; Curti-Martins, 2012, Cotta et al, 2022; Pellegrinetti et al, 2022).

The Pantanal is a low-lying region with a semi-humid tropical climate characterized by dry winter and rainy summer, controlled mainly by the South American monsoon (Zhou and Lau, 1998; Sakamoto et al., 2004; Furquim et al., 2008; Furian et al., 2013). The interaction between the regional rainfall pattern, the stock and the discharge of groundwater generates an annual evapotranspiration rate greater than that of precipitation (Hamilton et al., 1998; Alho, 2008; Guerreiro, 2016). Despite the negative annual water balance, precipitation in the rainy season is sufficient to leach the soluble species accumulated in the soil by evaporation in the dry season (Hamilton et al., 1998; INMET, 2020). The present-day rainfall regime does not explain the presence of alkaline soils and therefore, other processes must be considered.

Numerous studies carried out in the region over the past twenty years have ruled out the hypothesis that salinity is inherited from drier periods of the past, demonstrating that the saline-alkaline lakes are very probably isolated from the

surface drainage network. This disconnection would result in an endorheic-type system (Fig. 1): during the rainy season, saline-alkaline lakes are not flooded but only recharged by rainfall or lateral flow of groundwater; during the dry season, evaporation from the surface of the lake and by capillary rise from the surrounding soils concentrates the soluble species (Barbiero et al., 2002, 2008; Almeida et al., 2007; Furian et al., 2013). Some authors consider that lateral flow of fresh groundwater between lakes may continue during the dry season. The soils surrounding these lakes become alkaline, which results in values of soil electrical conductivity (ECs), pH and dissolved organic carbon (DOC) in soil water reaching 80 $dS.m^{-1}$, 11 and 750 $mgC.L^{-1}$, respectively (Mariot et al., 2007; Barbiero et al., 2008). They exhibit a number of characteristic features, in particular, the presence of deep, low-permeability green horizons, which are the sites of neoformation of specific secondary clay minerals, stevensite or Fe-illite (Barbiero et al., 2008; Furquim et al., 2008, 2010a, 2010b; Furian et al., 2013; Andrade et al., 2020; Vidoca et al., 2020; Souza Oliveira et al., 2021). The 3-D morphology of the green horizons may govern part of the lake groundwater dynamics (Sakamoto et al., 2004;

Barbiero et al., 2008; Furian et al., 2013; Freitas et al., 2019). Recent geochemical modeling has shown that 125 years of endorheic functioning are sufficient to reach the observed alkalinities (Merdy et al., 2022). These last authors noted that the alkaline character of the lakes and soils can disappear if new drainage conditions allow an export of the labile elements out of the system.

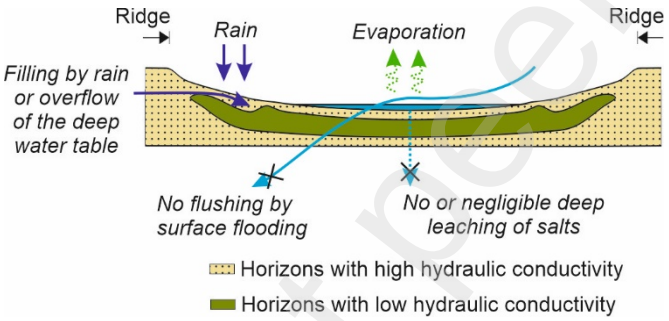

Fig. 1. Water dynamics - Main routes of water transfer in an alkaline lake according to the literature. (For colour the reader is referred to the web version of this article)

The results and interpretations presented above leave a few questions remaining. Firstly, the disconnection between saline-alkaline lakes and the surface drainage network, although very probable, has never been formally demonstrated by a long-term study. Another uncertainty is how does the alkalinization process begin, particularly the

146 waterproofing of green horizons? Finally, how is the saline-
147 alkaline lake type determined?
148 With this in mind, this study aims to characterize the
149 soil dynamics of a representative site under various factors
150 that may influence the geochemistry of saline-alkaline lakes.
151 The disconnection of the selected environments from
152 superficial drainage during different seasons, despite the
153 proximity of ephemeral recharge channels, suggests that the
154 soil, and more particularly its mineralogy, can act as
155 determinant factors for those types of environments and their
156 differences.

157 **2. MATERIAL AND METHODS**

158 **2.1. Lake selection**

159 Studied soils are located inside the Fazenda São
160 Roque (19º23'26" S and 56º19'33" W), in the municipality of
161 Aquidauana (Mato Grosso do Sul, Brazil) (Fig. 2). Four
162 saline-alkaline lakes were selected as representatives of the
163 southern subregion of the of Nhecolândia lacustrine system
164 following the testing of electric conductivity (EC_W), pH, E_H
165 and turbidity of each lake water (Table 1): one crystal-clear
166 water lake (7-Crystalline), two black water lakes (1-Black

167 and 6-Black) and one green water lake (4-Green) (Fig. 2).
168 Five freshwater lakes were also considered for spatial
169 analysis.

170 *Table 1. Saline-alkaline lake data*

171 *Parameters used to select representative saline-alkaline lakes within the*
172 *study site.*

	1-Black	***4-Green***	***6-Black***	***7-Crystalline***
Water Electrical	3500 (Jul/17)	3420 (Jul/17)	1662 (Jul/17)	826 (Sep/19)
Conductivity	3340 (Jul/17)	8730 (Sep/17)	28240 (oct/17)	
(EC_W - μScm^{-1})	8160 (Sep/17)	2990 (Sep/19)	1490 (Sep/19)	
	2270 (Sep/19)	3950 (Sep/19)	2050 (oct/19)	
		4990 (Sep/19)		
		5750 (oct/19)		
Water	31 (Jul/17)	27,4 (Jul/17)	26,6 (Jul/17)	25,5 (Sep/19)
temperature (ºC)	24,5 (Jul/17)	26,3 (Sep/19)	24,8 (Sep/19)	
Water pH	9,67 (Jul/17)	10,30 (Jul/17)	9,45 (Jul/17)	8,62 (Sep/19)
	9,70 (Jul/17)	9,76 (Sep/19)	9,24 (Sep/19)	
	9,35 (Sep/19)			
Water redox	+93,8 (Jul/17)	+88,9 (Jul/17)	+207,2 (Jul/17)	+50,0 (Sep/19)
potencial (mV)	+90,6 (Jul/17)	+88,7 (Jul/17)	+201,4 (Jul/17)	
	+88,3 (Jul/17)	-30,0 (Sep/19)	+192,1 (Jul/17)	
	-15,0 (Sep/19)		+90,0 (Sep/19)	
Sediment redox	-399,3 (Jul/17)	-408,5 (Jul/17)	-3,4 (Jul/17)	-280,0 (Sep/19)
potencial (mV)	-536,9 (Jul/17)	-418,3 (Jul/17)	-3,0 (Jul/17)	
		-430,0 (Sep/19)		

	-541,3 (Jul/17)		-9,7 (Jul/17)	
	-450,0 (Sep/19)		-220,0 (Sep/19)	
Turbidity (NTU)	28 (Jul/17)	>1000 (Jul/17)	117 (Jul/17)	1,8 (Sep/19)
	75 (Sep/19)	466 (Sep/19)	108 (Sep/19)	

Fig. 2. Location of study - Sites in the Nhecolândia area of the Taquari megafan, Pantanal, Brazil. Saline-alkaline lakes (1, 4, 6, 7) (B: black, G: green; C: crystalline) and freshwater lakes (F). T1 to T7: toposequences associated to the studied lakes. Satellite view from Google Earth. (For colour the reader is referred to the web version of this article)

2.2. Spatial data

Fluviometric data relied on the processing of 102 PlanetScope images on Google Earth Engine and ArcGIS 10.5 platforms, using supervised classifiers (Random Forest)

in a 45-month time series. The sensor system absorbs the reflectance of targets in the visible light spectrum, as well as in the blue (455-515 nm), green (500-590 nm) and red (590-670 nm) bands, in addition to near infrared (780-860 nm), resulting in 16-bit images of radiometric information (PLANET LABS, 2016). Orthorectified and atmospheric corrected (absence of clouds) 7x25 km images with a spatial resolution of 3 meters and with a passing time between 9:30 am and 11:30 am UTC, were selected fortnightly between October 2017 and July 2021. The study aimed to verify the disconnection of the studied saline-alkaline lakes from the surface drainage network. A quantitative value of 1 was assigned to pixels linked with the presence of water, the value of 0.5 for pixels associated with areas subject to seasonal flooding, and a 0 value for permanently dry areas. The flood frequency map was then obtained from a reducer (*'reduce.sum'*) applied over the entire image collection. Google Earth Engine reducers allowed the acquisition of statistical and arithmetic data as they operate across the stack of images that make up the time series (GOOGLE, 2020).

204 **2.3. Field work**

205 The soil characterization was carried out along
206 toposequences, following the Boulet et al. (1982) method.
207 The toposequences were positioned on the lake slopes in
208 regions of greater EC contrasts measured from the surface
209 with an EM38 electromagnetic conductivity meter (Geonics
210 Ltd, Canada), with the aim of observing the widest range of
211 soil variations. Microforms of local relief, lake levels and
212 drilling positions were obtained with greater that centimeter
213 precision from topographic data collected using the Global
214 Navigation Satellite System with Real-Time Kinematic
215 (GNSS-RTK) positioning. Soil macromorphological
216 characteristics were collected in boreholes drilled by manual
217 auger and cased to prevent collapsing. Soil colors were
218 obtained following Munsell (1954) references. When
219 possible, the depth, pH and CE_w of the water tables were
220 measured at the drilling time and 24 h after.

221 **2.4. Laboratory procedures**

222 Soil samples were dried in a ventilated drying oven
223 at 40º C, crushed and sieved with a 2-mm mesh to obtain
224 oven-dried fine earth (ODFE). When necessary, samples

were ground and sieved with a 150 mesh (106 μm) and/or organic matter was removed with sodium hypochlorite (NaClO) at pH 9.5 (Anderson, 1963), resulting in powder and organic matter free (OMF) aliquots. Particle size distribution was determined by the Robinson pipette method (Pansu and Gautheyrou, 2006) and textural classes were denominated according to the USDA (1987). Clay and silt fractions were obtained by centrifugation (Jackson, 1985). It should be noted that the mode of separation of the clay fraction, which requires suspension in ultrapure water, is likely to dissolve minerals such as evaporitic minerals or very small carbonates. Soil pH was measured from the ODFE with a 1:2.5 w:w soil:water ratio (EMBRAPA, 2017). Total chemical analysis for major element determinations was performed using total melting of soil samples and measured by Inductively Coupled Plasma Optical Emission Spectroscopy (ICP-OES).

2.5. Mineralogical analysis

Most soil minerals were characterized by X-ray Diffractometry (XRD) and Fourier Transform Infrared spectroscopy (FTIR). Diffuse Reflectance Spectroscopy

(DRS) was used for the identification of iron oxides and oxy-hydroxides. XRD samples were analyzed using a Philips PW 1877 diffractometer (Philips, Amsterdam, Netherlands) operated at 40kV potential, 40mA current, using CuKα radiation with a graphite crystal monochromator. The scan was performed from 3º to 90º (2θ) with a step of 0.02° and 2,5 seconds per time accumulation step. Mineral phases were identified on the X' Pert HighScore Plus version 4.9 software (Malvern Panalytical, Netherlands). XRD analysis was performed on the clay fraction (<2 μm) from the ODFE and OMF aliquots, oriented and saturated (1) with magnesium chloride ($MgCl_2$), later solvated with ethylene glycol (EG), and (2) with potassium chloride (KCl), later heated to 110 and 550 ºC (Wilson, 1987).

Representative peaks used for mineral identification were the following: quartz, 3.34Å, 4.25Å and 1.81Å; feldspars (microcline and/or orthoclase), 3.24Å, 4.21Å and 3.29Å); micas (muscovite and/or illite), 4.29Å, 3.86Å and 10Å; kaolinite, 7.13Å, 3.56Å and 4.35Å; 2:1 expandable clay minerals (montmorillonite and/or vermiculite), 12 to 15Å; calcite, 3.02Å, 1.87Å and 2.28Å.

FTIR was performed on OMF clay mixed with potassium bromide (KBr) pellets prepared with KBr Tablet Die using a Shimadzu IR Prestige-21 spectrophotometer (Shimadzu, Japan), with spectra from 400 to 4600 cm^{-1}. Saturation or low-resolution bands were re-evaluated in replicates with lower or higher sample mass pellets. Normalization of results was achieved by the mineral phase band with the highest absorption, considering an absorbance correction factor based on mass values of sample, KBr and pellets. The identification of mineral phases was performed by characteristic absorption bands (Russel and Fraser, 1994; Ekosse, 2005; Vaculíková and Plevová, 2005; Saikia et al., 2008; Ji et al., 2009; Theodosoglou et al. 2010; Lainé et al., 2017; Acevedo et al., 2017; Zviagina et al., 2020).

The identification of iron oxides and oxy-hydroxides by DRS was performed on powder ODFE and OMF clay in a Cary 5 spectrometer (UV-VIS-NIR) (Varian, USA). The samples were analyzed in triplicate, ranging from 370 to 820nm with increments of 0.1nm. The reflectance R was measured in comparison to a Halon pattern and transformed into the Kubelka-Munk remission function [$f(R) = (1 – R)^2 / 2 R$]. From the obtained curves, the second derivative was

calculated and mineral phases were identified through characteristic absorption bands ^4E:^4A_i and EPT (Electronic Pair Transition) (Kosmas, 1984; Malengreau et al., 1996; Scheinost et al., 1998; Cornell and Schwertmann, 2000). Identification of goethite and hematite was made by comparison with characteristic absorption bands in commercial standards (Sigma-Aldrich 71063 and 310050, respectively).

2.6. Statistics

Principal components analysis (PCA) was performed using XLSTAT 2017 on various sets of the obtained data. PCA project multidimensional data clouds to subspace in order to minimize the residual variance, choosing the most relevant directions (principal components) in the data (Jolliffe 2002). We chose a correlation based PCA on standardized variables to avoid sensitivity to the scaling of the variables.

3. RESULTS AND DISCUSSION

3.1. Study site and lake characteristics

The fieldwork was carried out at the end of the dry season, which is the time of year when motorized land access to the study site is possible, in October 2017,

September 2018, October 2019 and November 2020. During collection of soil samples, physicochemical parameters of waters and sediments from within the selected saline-alkaline lakes (Fig. 1) were monitored and are presented in Table 1. The crystalline-type lake and the green-type lake had the lowest and highest pH and turbidity values, respectively, the black-type lakes being in between. Significant EC_w variations were observed according to time period, ranging from 826 µS/cm (7-Crystalline lake on September 2019) to 28240 µS/cm (6-Black lake on October 2017).

The alkaline lakes showed a typical succession of vegetation from their upper part to their lower part: *cerrado* type savanna forest on the sandy ridges and a succession of savanna woodland, open woody savanna, open shrubby grassfield with palm trees and savanna grassfield on the slopes, susceptible to differentiation by the predominance of *andropogon bicorns* (*capim-de-burro*) and *cynodon dactylon* grass species (Salis et al., 2014) (Fig. 3).

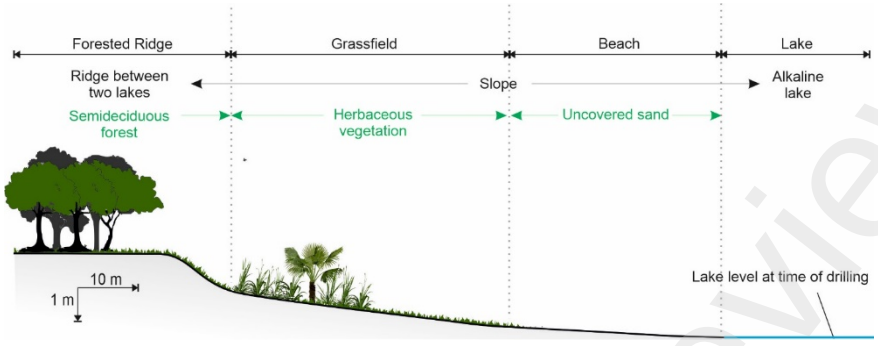

Fig. 3. Landscape units - Typical vegetation along a saline-alkaline lake slope.

The lake biota differed between lake types (Pellegrinetti et al., 2022). It was oligotrophic vegetated for the 7-Crystalline lake, oligotrophic turbid for the 1-Black and 6-Black lakes, and eutrophic for the 4-Green lake

3.2. Spatial Analysis

The 102 PlanetScope satellite images showed that the four studied saline-alkaline lakes are all surrounded by forested sandy ridges, the altitude of which is more than 2 m higher than the surface of the lakes at the end of the wet season (Fig. 4). Although all taken in the same season, the views show significant variations in the levels of the lakes, resulting from the rainfall of previous months. In October 2019 (Fig. 4B), the lakes had a rather high water level for the end of the dry season due to regular rainfall in the previous

rainy season. In November 2020 (Fig. 4C), the lakes had very low water levels, with some almost dry, due to low rainfall in the previous rainy season. The situation was intermediate in October 2017 (Fig. 4A). These observations underline the strong interannual heterogeneity of precipitation.

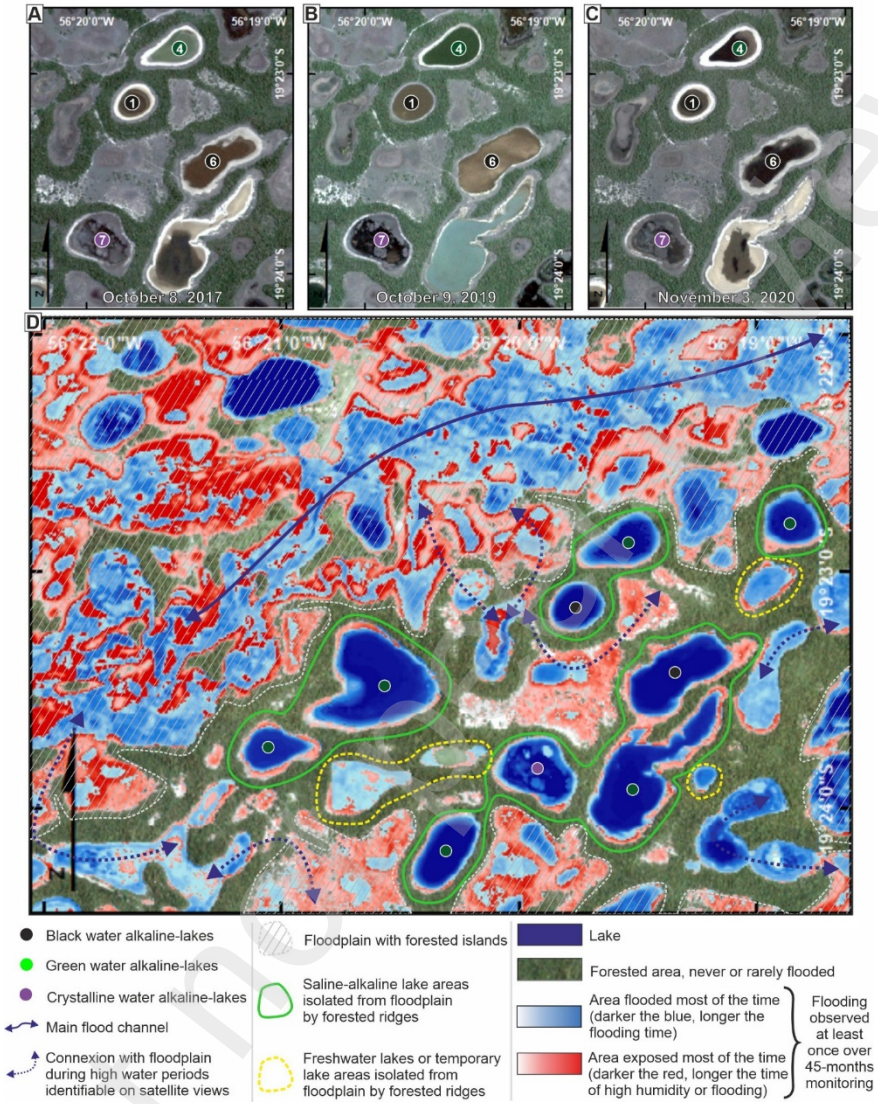

Fig. 4. Flooding monitoring - Interannual variability of the water level in the lakes studied. Satellite views from PlanetScope. (For colour the reader is referred to the web version of this article).

The flooding dynamics in the area are outlined in Fig. 4D. Patches of lighter blue tones inside the 7-Crystalline lake are due to the presence of macrophytes and their

spectral reflectance characteristics. The ephemeral flood channels, regionally called *vazantes*, follow the geomorphological description of Cunha (1980) of smooth and elongated depressions that distribute the incoming floods, thus corresponding to periodically flooded soils. The main flood channel of the area (called *Mangabal vazante*) is connected with the Taquari River and responsible for the terrestrial surface recharge of freshwater lakes during the rainy season (plain line arrow; Fig. 4). For most freshwater lakes located outside the floodplain, it is possible to identify temporarily active connections with the floodplain (dotted arrows; Fig. 4). Some freshwater lakes, however, are surrounded by forested ridges with no identifiable connection to floodplains. As for the hypothesis to which the saline-alkaline lakes would result from a disconnection with the superficial hydrographic network, this shows that the mere presence of a forested ridge is insufficient to ensure such a disconnection.

Levels of saline-alkaline and freshwater lakes measured during the same day in November 2019 are given in Fig. 5B. The same elevation of freshwater lakes could indicate a regional water table level; the different elevation of

381 the alkaline lakes could indicate a hydraulic disconnection of
382 these lakes with regional groundwater (Fig. 5).

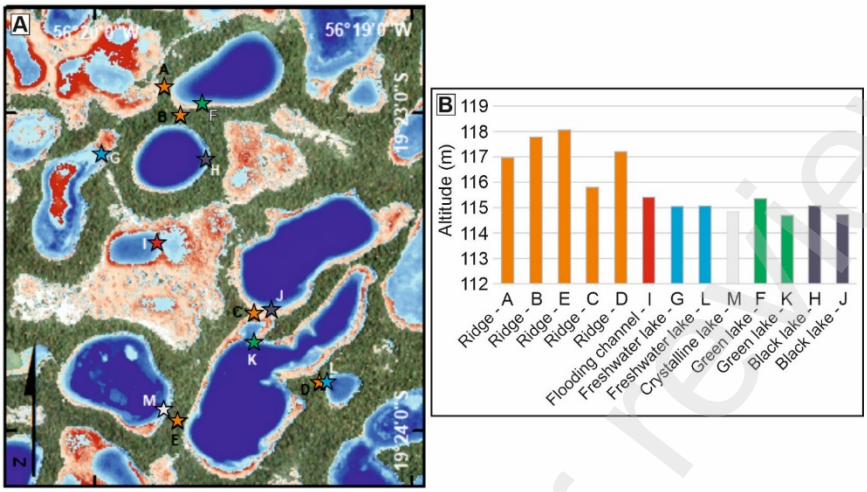

383

384 *Fig. 5. Topographic data - Altitude of ridges and lake levels measured on*
385 *the same day. Letters refer to points situated on the satellite view. (For*
386 *colour the reader is referred to the web version of this article).*

387 **3.3. Toposequences**

388 EC_S mapping around toposequences and borehole
389 locations are given in Fig. 6. Several factors can result in
390 higher EC values, such as soil moisture, clay content, and
391 concentration of ionic species in the soil solution (Alves et
392 al., 2013). For better visualization, the EC_S profiles along
393 each toposequence will be shown in toposequence figures
394 (red lines on Figs. 8 to 11).

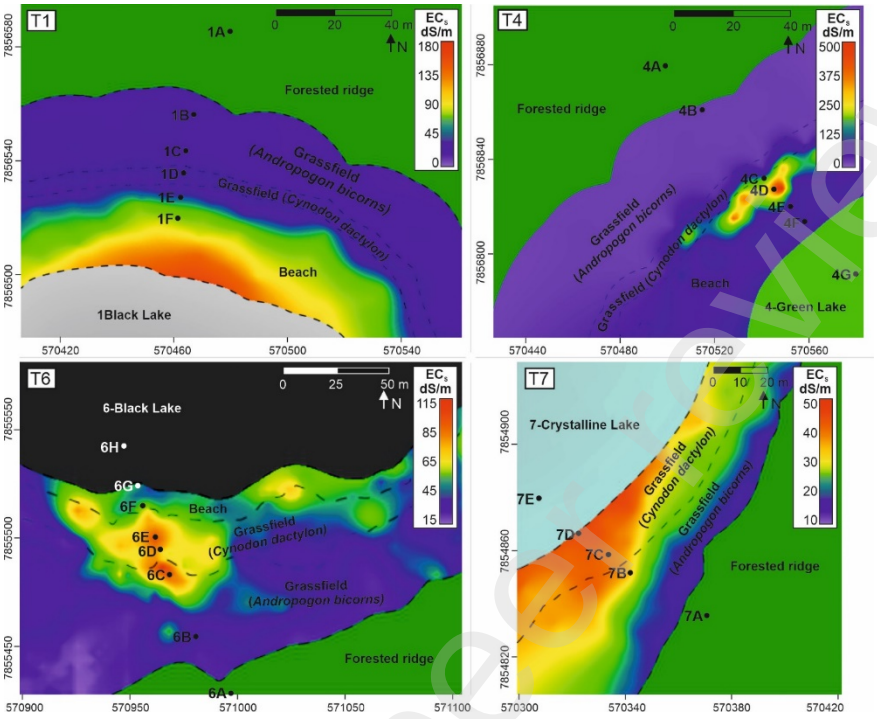

395

396 *Fig. 6. Apparent electrical conductivity mapping of soils – EC_S values*
397 *around each saline-alkaline lake selected, with the delimitation of*
398 *different landscape unit areas and the positioning of all boreholes. (For*
399 *colour the reader is referred to the web version of this article).*

400 The nomenclature of the horizons is made according
401 to their dominant color and their texture, following the rules
402 presented in Fig. 7, with notes being taken about horizons
403 with heterogeneous colors, varied nodules, and spots
404 associated with organic matter. Details about borehole
405 positioning, depths, particle size distribution and pH in water
406 for all samples are available as supplementary material.

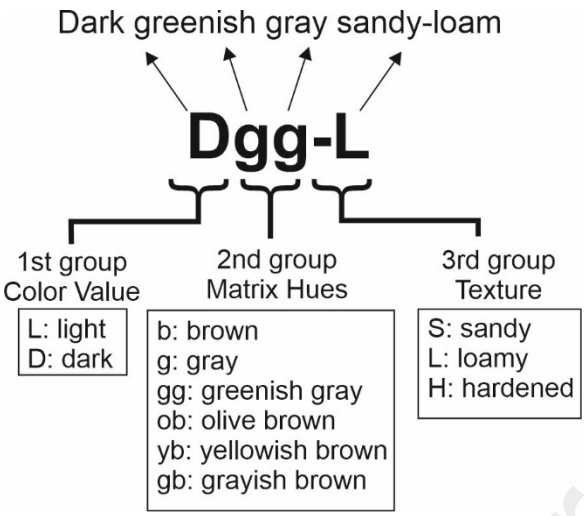

407

408 *Fig. 7. Nomenclature of the horizons – Scheme of the different color*

409 *values, matrix hues and textures found in the studied soils.*

410 ### *3.3.1. T1-Black lake toposequence (Fig. 8)*

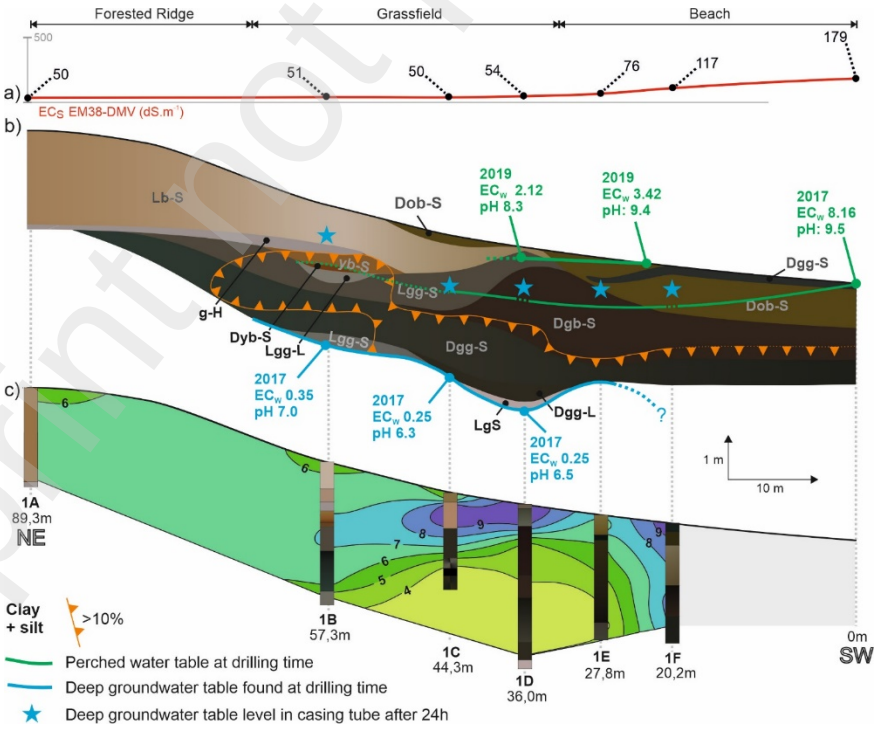

411

Fig. 8. T1 - Main characteristics of the 1-Black lake toposequence. (a) EC_S profile; (b) soil horizons, water levels, fine fraction and EC_W values; c) soil pH. (For colour the reader is referred to the web version of this article).

The ridge soil was a homogeneous, sandy, light brown profile more than 2 m deep overlying a g-H indurated silcrete horizon that prevented manual drilling. Such silcrete are known to form by Si liberation by silicate weathering, followed by its precipitation as secondary silica driven by supersaturation promoted by evaporation in the capillary fringe (Nash and Ullyott, 2007). The geochemical feasibility of this process in the considered soil has been confirmed by modeling (Merdy et al., 2022). Downslope, this silcrete horizon progressively turned less indurated and disappeared, with the whole profile becoming darker and greener. The deep horizons, although remaining sandy, gradually became loamier, up to 17.6% of (clay + silt) at the base of the slope. These loamier horizons had low hydraulic conductivity, as evidenced by the two different water tables observed during the surveys: a perched water table with high EC_W and pH (higher than 2.1 mS cm^{-1} and 8.2, respectively), and a deep-water table with low EC_W and pH (lower than 0.4

mS cm^{-1} and 7.1, respectively). The deep-water table was under hydraulic load: water slowly raised in the casing tube after it was reached. The low-permeability green horizons formed a marked step on the slope, favoring the hydraulic discontinuity between the ridge and the soils of the lower slope.

Soil pH (Fig. 8c) ranged from 3 to 10 within the toposequence. Ridge soil was slightly acidic, around 6-7. Topsoil horizons gradually became more alkaline downstream, reaching values greater than 9 in the lower part of the slope, which was consistent with the gradual increase of EC_S. Very acid horizons (hyperacidic horizons, pH < 4) were observed at depth in the lower third of the slope.

Horizon geometry and characteristics, including pH contrast, have already been observed in similar toposequences (Barbiero et al., 2008, 2016). Based on geochemical modeling, the pH contrast was attributed by Merdy et al. (2022) to the mixing of alkaline water from downslope surface horizons and deep acidic groundwater.

3.3.2. T4-Green lake toposequence (Fig. 9)

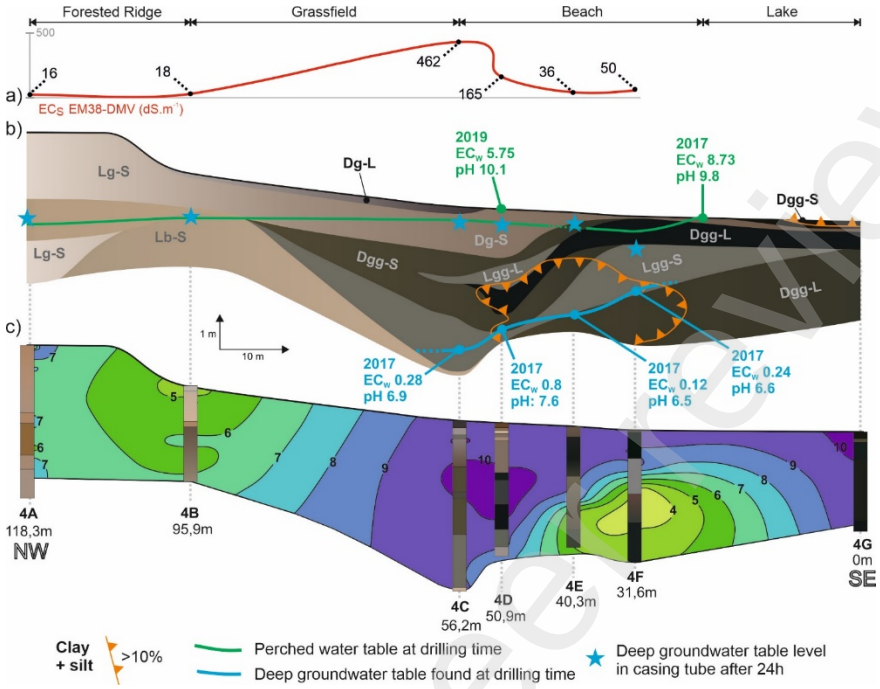

454

455 *Fig. 9. T4 - Main characteristics of the 4-Green lake toposequence. (a)*
456 *EC_S profile; (b) soil horizons, water levels, fine fraction and EC_W values;*
457 *c) soil pH. (For colour the reader is referred to the web version of this*
458 *article).*

459 The T4 toposequence was very similar to the T1
460 toposequence: from the upper to the lower part of the slope,
461 the profile progressively darkens and turns greener; (clay +
462 silt) content increase in depth forming low hydraulic
463 conductivity horizons isolating an alkaline perched water
464 table from acidic deep groundwater; topsoil pH increases
465 gradually up to 10.5; and there are hyperacidic horizons at
466 depth in the lower third of the slope. There were, however,

some differences: no indurated silcrete was observed at depth in the ridge soil; the EC_S profile showed high values towards the middle of the slope, which could be due to a local higher accumulation of salts in topsoil horizons by capillary rise of the lake water.

3.3.3. T6-Black lake toposequence (Fig. 10)

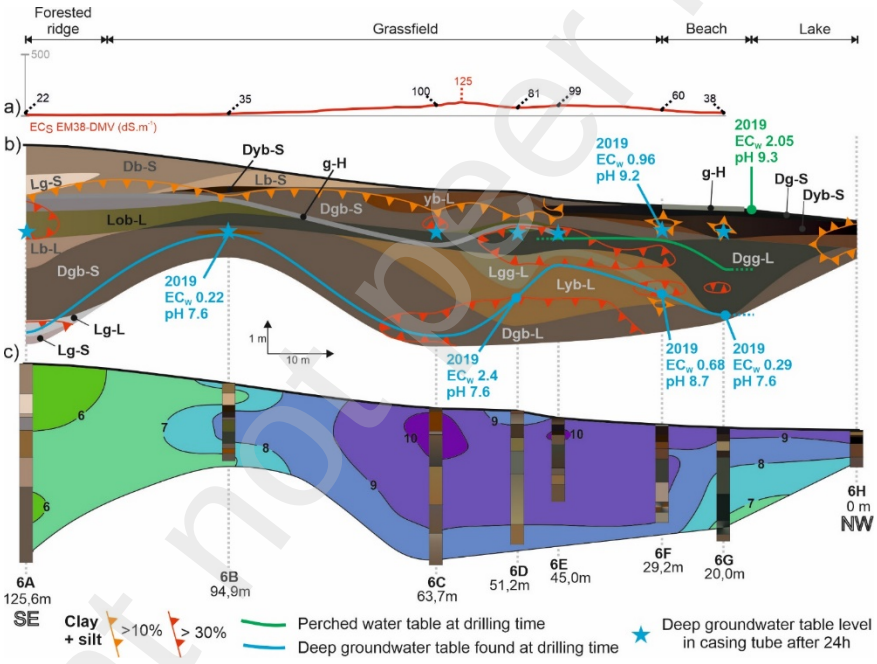

Fig. 10. T6 - Main characteristics of the 6-Black lake toposequence. (a) EC_S profile; (b) soil horizons, water levels, fine fraction and EC_W values; c) soil pH. (For colour the reader is referred to the web version of this article).

Most of the similarities between T1 and T4 toposequences were observed in the T6 toposequence:

horizon color transitions, (clay + silt) content increase forming low hydraulic conductivity horizons that isolate different water tables and a gradual increase of the topsoil pH. However, some features differed. The deep groundwater was slightly less acidic (around 7.6), which could indicate less impermeable green horizons. The whole sequence had a higher (clay + silt) fraction content, which could be due to a higher fine fraction content of the parent material, as suggested by a (silt + clay) content higher than 30%, 550 cm deep, in the ridge soil. A well-developed hardened silcrete horizon was observed around 150 cm in depth from the ridge to the lower third of the slope and discontinuous topsoil silcrete horizons were also observed along the lower third of the slope. Better development of silcrete compared to the T1 toposequence could be due to higher capillary rise due to the higher content of the fine fraction or, regarding the ridge silcrete, a flow-barrier effect due to textural layering (Li et al., 2014). The EC_S profile along the slope presented multiple peaks, which could be related to textural variations in the topsoil horizons. Acidic, not hyperacidic, horizons were observed at depth in the lower part of the toposequence, which can be due to less impermeable green horizons

allowing better mixing between alkaline and acid groundwaters and better water turnover. It is also possible that the observations were not deep enough to observe hyperacidity.

3.3.4. T7-Crystalline toposequence (Fig. 11)

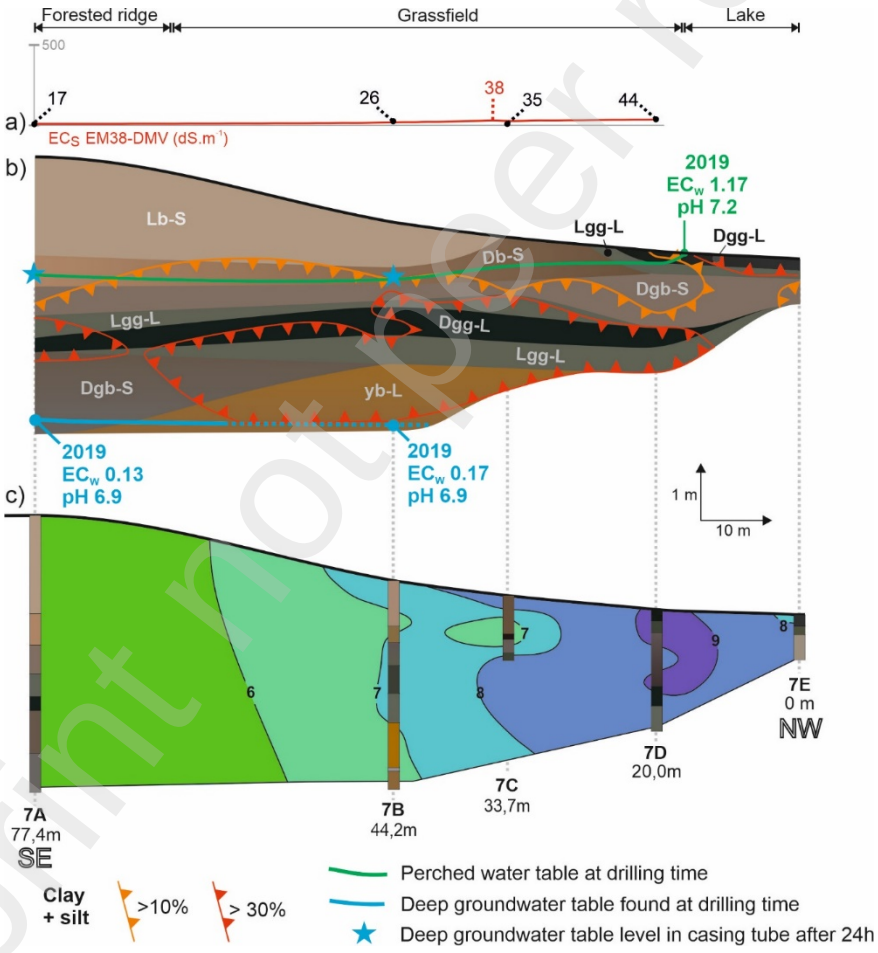

Fig. 11. T7 - Main characteristics of the 7-Crystalline lake toposequence. (a) EC_S profile; (b) soil horizons, water levels, fine fraction and EC_W

values; c) soil pH. (For colour the reader is referred to the web version of this article).

The T7 toposequence ends on a less alkaline lake than the others, with the presence of shells on the beach surface and subaerial vegetation inside the lake. Like the other three toposequences, this one had soils ranging from acidic to alkaline horizons from the ridge to the lake and two distinct water tables separated by greenish horizons. The poorly permeable green horizons, however, did not form a marked step on the slope. The hydraulic discontinuity between the ridge soils and the upper soil horizons at the lower part of the slope is therefore less marked than for the other sequences. The downslope soils were slightly less alkaline than in other toposequences, with the maximum measured pH being 9.2. Consistently, the pH of the perched water table measured in 2019 had a lower EC_W value (1.1 mS cm^{-1}) than in other toposequences and was only slightly alkaline (7.2), with little difference with the deep groundwater (6.9). No hyperacidic horizons were observed at depth in the lower part of the toposequence. As for toposequence T7, the soils showed, on average, a higher fine fraction content than toposequence T1 and T4. As for the T7 toposequence, the

less intense peaks in the ECs profile along the slope could be related to horizons with less salt accumulation, in which less textural variations in the topsoil horizons causes less confinement.

3.4. Mineralogy results

A summary of main minerals identified by XRD, FTIR and DRS is given in Fig. 12. The main minerals identified along the toposequences were quartz, feldspars (microcline and/or orthoclase), micas (muscovite and/or illite), kaolinite, 2:1 expandable clay minerals (montmorillonite and/or vermiculite), calcite, goethite, hematite, ferrihydrite.

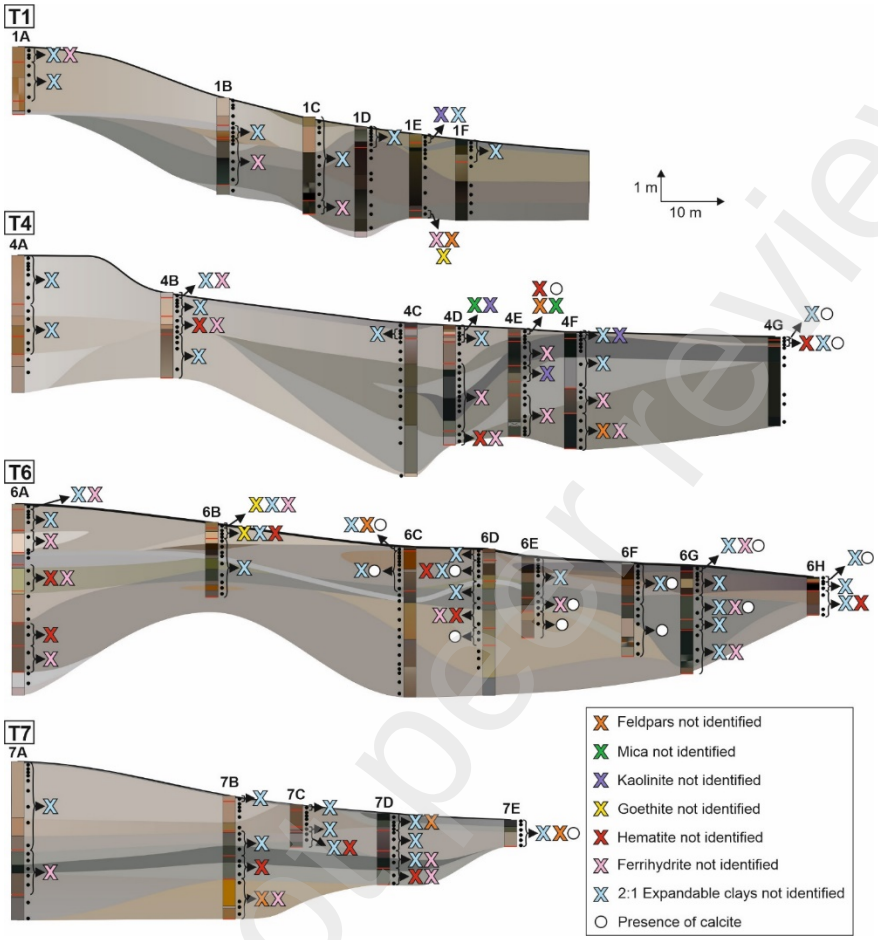

543

544 *Fig. 12. Soil mineralogy - Main minerals along the sequences. Black*
545 *points indicate the analyzed samples. Unless otherwise stated, the*
546 *following minerals have been identified at each point: quartz, feldspars,*
547 *micas, kaolinite, 2:1 expandable clay minerals, goethite, hematite,*
548 *ferrihydrite. The figure therefore represents the absence of one or more*
549 *of these minerals or the presence of calcite. (For colour the reader is*
550 *referred to the web version of this article).*

551 Quartz, feldspar and muscovite, part of illite and
552 kaolinite are inherited from the parent sediment. These

minerals were likely transported with little modification and remained restricted to the sand and silt fractions (Assine et al., 2015; Oliveira Júnior et al., 2020).

According to published studies on similar systems (Barbiero et al., 2008, 2016; Furquim et al., 2008, 2010a, 2010b; Guerreiro et al., 2019; Andrade et al., 2020), the main expected secondary minerals are Fe-kaolinite, Fe-illite, Fe-beidellite-type smectite in upslope soils, stevensite-type smectite in downslope soils, with many types of mixed-layered types from these phyllosilicate species, amorphous silica which can form silcrete nodules or horizons, and calcite. In this study we did not differentiate illite from muscovite, or types of expandable 2:1 clays. We have however noticed that expandable clays were present everywhere, except in the sandiest horizons of the upper part of the profiles. On ridges, this was expected in the leached, acidic sandy horizons where there are no conditions for the neoformation of 2:1 secondary clay minerals. On slopes, where higher pH and local carbonate precipitations attest to more confined conditions, possibly precipitated 2:1 minerals may be leached at depth or downstream by perched groundwater circulation.

Calcite was observed in high pH downslope horizons, especially in the T6 toposequence, where HCl-effervescent nodules larger than 2 mm were observed. Calcite in the other green horizons could however have been ignored due to the method of separation of the clay fraction during which soluble minerals can be dissolved (§2.4). Calcite nodules support the hypothesis of concentration of solutes by dry season evaporation of groundwater presumably from the lake or from deeper horizons.

Amorphous silica was not identified by XRD, but its presence is most likely based on observations of hardened horizons (g-H) or non-HCl-effervescent nodules (horizons Dgg-L and Lgg-L).

These results are consistent with the results obtained by Merdy et al. (2022) using conceptual geochemical modeling on an idealized toposequence similar to those described here. While kaolinite precipitation is generally associated with wetter climates (Ishida et al., 2014), this remains possible here despite the strongly negative annual water balance. These authors, however predict, in the downslope surface horizons,that there is precipitation of evaporitic minerals (gaylussite, pirssonite,

sylvite, nahcolite, halite, glaserite), none of which were observed in our study. Here too, the mode of preparation of the clay fraction is probably responsible for the non-observation of these very soluble minerals.

With regard to iron oxides and hydroxides, we did not observe in the results obtained here a correlation of their distribution with other characteristics nor a causality in this distribution. Goethite and hematite are common phases in soils, as a result of Fe-rich silicates weathering processes and may even act as a reliable proxy for local precipitation (Zhang et al., 2007). While hematite can be associated with hot and dry environments, goethite can be associated with cold and humid environments. Ferrihydrite ($Fe^{3+}_2O_3$*$0.5H_2O$) is a metastable mineral that marks the first precipitation stage in iron oxidation during hydrolysis, which may transform via the hematite or goethite transformation pathways depending on pH and moisture. Such transformations occur simultaneously, either by the condensation of ions or crystal dissolution in acidic (pH 3 to 4) and alkaline (pH > 8) conditions forming goethite, or by dehydration and internal atomic rearrangement of solid ferrihydrite in a neutral pH favoring hematite formation

(Schwertmann et al., 1999; Cudennec and Lecerf, 2006). In the studied toposequences, such dynamics were not detected between hyperacid (pH < 4) and alkaline zones.

3.5. Chemical results

The average of all samples demonstrates the following succession: silica (SiO_2 = 91.84%), aluminum (Al_2O_3 = 2.22%), iron (Fe_2O_3 = 1.75%), potassium (K_2O = 0.75%), calcium (CaO = 0.30%), magnesium (MgO = 0.21%), titanium (TiO_2 = 0.18%), sodium (Na_2O = 0.11%), manganese (MnO = 0.11%) and phosphorus (P_2O_5 = 0.01%). The great dominance of SiO_2 is due to the high content of quartz sand in all samples. Relationships between the elements and the soil material texture and pH can be discussed from the PCA results (Fig. 13).

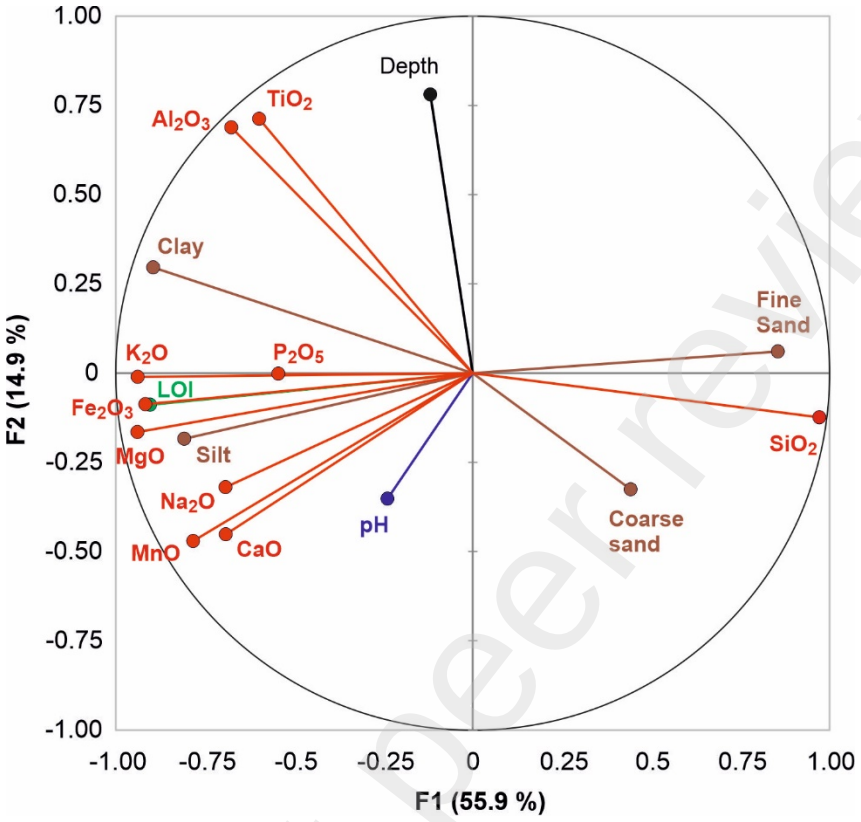

633

634 *Fig. 13. Statistical data - PCA correlation circle between variables.*

635 *Percentage on each factorial axis gives the explained variance. LOI: loss*

636 *on ignition.*

637 The first factorial axis is mainly defined by SiO_2 and

638 sand on one side, and clay, silt and other elements on the

639 other side. This is consistent with the differentiation between

640 very sandy horizons and horizons with the presence of clay,

641 often associated with other minerals (calcite, iron oxides).

642 The second factorial axis is mainly defined by depth, Al_2O_3

643 and TiO_2 on one side, opposed to pH, CaO, MnO and Na_2O

644 on the other side. The negative correlation between pH and
645 depth is driven by high pH surface horizons near the lake
646 and hyperacidic horizons at depth in the T1 and T4
647 sequences. The axis probably also differentiates acidic
648 horizons richer in aluminous 1:1 clays (kaolinite) as indicated
649 by the Al_2O_3 point, alkaline horizons richer in less aluminous
650 2:1 clays with K, Fe or Mg (Fe-illite, stevensite) as indicated
651 by the K_2O, Fe_2O_3 and MgO points and evaporitic horizons
652 as indicated by the Na_2O and the CaO points.

653 **3.6. Possible active processes**

654 The granulometric, mineralogical and chemical
655 differences in the soils observed along each toposequence
656 are the result of neoformation, precipitation, dissolution,
657 transformation, dehydration and mineral heritage acting on
658 the site (Macias and Camps, 2020; Vidoca, 2020), all
659 dependent on physicochemical properties of the soil
660 solutions.

661 *3.6.1. Pedogenesis, hydrodynamics and lake type*

662 The observed mineralogy reflects particularities of
663 the Nhecolândia environment. Firstly, that there is a
664 predominance of sandy materials, therefore very siliceous,

with low levels of aluminum and good permeability. Secondly, the contrasting climate allows both a leaching environment during the rainy season with solute supply in lakes, and a confined environment during the dry season with solute accumulation in lakes and downslope soils. Annual precipitation and potential evapotranspiration in the region (averages of 1100 and 1400 mm, respectively) result in a negative water balance (Alho, 2008). However, during rainy seasons, precipitation exceeds potential evapotranspiration by about 200 mm and, consequently, a water deficit of about 500 mm is maintained during the dry season (Hamilton et al., 1998). Thirdly, the fluctuations in water levels throughout the climate cycle are decisive. For freshwater lakes (*baías*), high water levels during the rainy season allows flushing towards main watercourses, of the solutes accumulated during the rainy season. Two non-exclusive processes can lead to flushing: lake overflow or deep leaching through groundwater (Sakamoto et al., 2004). Saline-alkaline lakes can form when low-permeability horizons allow hydraulic disconnection between deep groundwater on one hand, and lakes and downslope perched water-tables on the other. Here we confirmed the

687 presence of such horizons in each of the studied
688 toposequences. We observed consistency between (1) the
689 distribution of greenish, more clayey horizons and (2) the
690 disconnection between an alkaline, perched groundwater
691 and an acidic, deep groundwater. An overflow of non-
692 alkaline groundwater continuing to feed the saline-alkaline
693 lake during the dry season, as hypothesized by Costa et al.
694 (2015), was not observed. On slopes, the greenish horizons
695 formed a step favoring endorheism in T1, T4 and T6. A step
696 was less visible in T7. It is therefore possible that the
697 hydraulic isolation of the T7 crystalline lake has been less
698 effective than for the other lakes, which could explain a lower
699 confinement resulting in a lower alkalinity, attested by a
700 lower ECw and pH of the lake waters. These would neither
701 reach the threshold for triggering an algal bloom as in the
702 green lakes, nor the threshold for massive solubilization of
703 organic matter as in the black lakes.

704 *3.6.2. Hydrodynamics and mineral genesis*

705 The type of minerals observed at the sequence
706 scale was closely related to hydrodynamics that impacts the
707 chemistry of the groundwater. The minerals observed here

where feldspar, 1:1 clays, non-expandable 2:1 phyllosilicate, expandable 2:1 clays, secondary silica, iron oxides and calcite. The mineral distribution observed at the toposequence scale is consistent with studies conducted in similar systems (Barbiero et al., 2008, 2016; Furquim et al., 2008, 2010a, 2010b). On the ridges, leached sandy horizons overlie horizons in which there is dissolution of primary minerals and neoformation of minerals 1:1 (Fe-kaolinite) and 2:1 (Fe-illite, Fe-beidellite). The greenish horizons on downslopes were formed by neoformations characteristic of confined environments (stevensite like clays, calcite). Our data provide new insights into the precipitation conditions of secondary silica. Secondary silica forming silcrete materials can form when there is not enough Al with regard to Si to allow phyllosilicate precipitation (Taylor and Eggleton, 2017). Here silcrete were observed (1) below the leached sandy horizons, on the ridge and in the upper part of the slope, or (2) on the topsoil, downslope. The first type of silcrete was formed in acidic (pH < 7), sandy material. Silica precipitated from a soil water concentrated by evaporation in the capillary fringe, the low Si/Al ratio being likely since the percolating rainwater only encountered very sandy materials. The

second type of silcrete was formed in alkaline (pH > 9) material. Silica was precipitated from lake water transferred by capillarity and concentrated by evaporation. In this environment, the high Si/Al ratio is also favored by the high pH of the lake water that increases the quartz solubility and the quartz dissolution rate. The quartz dissolution rate is increased by 10 times at pH 9.5 compared to pH 7 (House and Orr, 1992) and by more than 20 times at the ionic strength of lake water compared to rainwater (Icenhower and Dove, 2000). As a result, the black lake water concentrations of dissolved Si and Al average about 1.1 10^{-1} and 1.5 10^{-4} ml L^{-1}, respectively (Merdy et al., 2022). There are therefore two types of silcrete in such systems, one formed under neutral/acidic conditions, the other under alkaline conditions, both formed in an evaporating capillary fringe.

4. CONCLUSIONS

This research marks the initial stage of the studies of factors that determine the dynamics between different types of saline-alkaline lakes and nearby surrounding soils. The objective of verifying, on a single site, a set of results previously acquired by independent studies on many distinct

751 Nhecolândia sites has been partially achieved. Our results
752 confirmed the general organization of the soil cover around
753 saline-alkaline lakes. The very sandy light brown soils of the
754 ridges, which eventually present a silcrete type horizon at
755 depth, give way down the slopes to greenish soils with, at
756 depth, more clayey horizons with low permeability. These
757 establish a hydraulic discontinuity between the slightly acidic
758 groundwater of the general, deep groundwater and the very
759 alkaline perched groundwater. Our 45-month time sequence
760 of satellite data confirmed that the studied saline-alkaline
761 lakes remained isolated from the ephemeral superficial flood
762 channels. Some freshwater lakes, however, also remained
763 isolated, which shows that the leaching of labile elements
764 out of the lake catchment can occur via other processes than
765 surface flushing, such as deep drainage or groundwater
766 flushing. This shows that hydraulic discontinuity between
767 surface groundwater on lake slopes and deep groundwater
768 is a necessary condition for the acquisition of the saline-
769 alkaline character of the lakes. Our results also suggested
770 that some saline-alkaline lakes may remain crystalline due to
771 slightly lower alkalinity as a result of less efficient hydraulic
772 discontinuity between deep groundwater and alkaline lake

and soil water. The alkalinity of crystalline lakes would remain too low to allow a cyanobacteria bloom or the maintenance of organic matter in solution.

The present study confirmed the presence and location on the slopes of hyperacidic horizons, located downslope beneath the more alkaline horizons. Modeling by Merdy et al. (2022) showed that a pH between 3.2 and 3.5 can be achieved by mixing water from alkaline horizons or lakes and deep groundwater, with the reduction in pH attributed to ferrolysis. The validation of such a mechanism will however require more detailed mineralogical investigations. It also remains to verify the mineralogy of 2:1 minerals associated with deep ridge soil horizons and slope alkaline horizons.

DECLARATION OF INTERESTS

The authors declare that they have no known competing financial interests or personal relationships that could have appeared to influence the work reported in this paper.

DATA AVAILABILITY

Raw data is given as supplementary material.

ACKNOWLEDGEMENTS

This work was supported by the São Paulo Research Foundation (FAPESP) [grant numbers #2016/14227-5 and #2019/21157-1] and the Brazilian National Council for Scientific and Technological Development (CNPq) [grant number CRM #307024/2018-0].

REFERENCES

Acevedo, N.I.A., Rocha, M.C.G., Bertolino, L.C. 2017. Mineralogical characterization of natural clays from Brazilian Southeast region for industrial applications. Cerâmica, 63, 253-262. http://dx.doi.org/10.1590/0366-69132017633662045

Alho, C. J. R., 2008. Biodiversity of the Pantanal: response to seasonal flooding regime and to environmental degradation. Braz. J. Biol. 68 (4 suppl), 957–966. https://doi.org/10.1590/S1519-69842008000500005

Almeida, T. I. R. A., Fernandes, E., Mendes, D., Branco, F.C., Sígolo, J.B., 2007. Distribuição espacial de diferentes classes de Lagoas no Pantanal da Nhecolândia, MS, a partir de dados vetoriais e SRTM:

uma contribuição ao estudo de sua compartimentação e gênese. Geologia USP. v 7, n 2. https://doi.org/10.5327/Z1519-874x2007000200007

Alves, S.M.F., Alcântara, G.R., Reis, E.F., Queiroz, D.M., Valente, D.S.M., 2013. Definição de zonas de manejo a partir de mapas de condutividade elétrica e matéria orgânica. Biosciencia Journal, Uberlândia, v. 29, p. 104-114. Available from: https://seer.ufu.br/index.php/biosciencejournal/article/view/13687.

Anderson, J.U., 1963. An improved pretreatment for mineralogical analysis of samples containing organic matter. Clays Clay Miner. 10, 380–388. https://doi.org/10.1346/CCMN.1961.0100134

Andrade, G.R.P., Furquim, S.A.C., Nascimento, T.T.V., Brito, A.C., Camargo, G.R., Souza, G.C., 2020. Transformation of clay minerals in salt-affected soils, Pantanal wetland, Brazil. Geoderma. 371, 114380. https://doi.org/10.1016/j.geoderma.2020.114380

833 Assine, M.L., Merino, E.R., Pupim, F.N., Warren, L.V.,
834 Guerreiro, R.L., McGlue, M.M., 2015. Geology and
835 Geomorphology of the Pantanal Basin. In: Bergier, I. and
836 Assine, M. L. (Eds.) Dynamics of the Pantanal Wetland in
837 South America, pp. 23-50.
838 https://doi.org/10.1007/698_2015_349

839 Barbiero, L., Queiroz-Neto, J.P., Ciornei, G., Sakamoto,
840 A.Y., Capellari, B., Fernandes, E., Vallès, V., 2002.
841 Geochemistry of water and ground water in the
842 Nhecolândia, Pantanal of Mato Grosso, Brazil: variability
843 and associated processes. Wetlands 22 (3), 528–540.
844 https://doi.org/10.1672/0277-
845 5212(2002)022[0528:GOWAGW]2.0.CO;2.

846 Barbiero, L., Rezende-Filho, A.T., Furquim, S.A.C., Furian,
847 S., Sakamoto, A.Y., Vallès, V., Graham, R.C., Fort, M.,
848 Ferreira, R.P.D., Queiroz-Neto, J.P., 2008. Soil
849 morphological control of hydrogeochemistry in a saline
850 and freshwater lake landscape in the Pantanal of
851 Nhecolândia, Brazil. Geoderma, 148, 91-106.
852 https://doi.org/10.1016/j.geoderma.2008.09.010

853 Barbiero, L., Berger, G., Rezende Filho, A.T. Meunier, J-F.,
854 Martins-Silva, E.R., Furian, S. 2016. Organic Control of
855 Dioctahedral and Trioctahedral Clay Formation in an
856 Alkaline Soil System in the Pantanal Wetland of
857 Nhecolândia, Brazil. PLoS One, Jul 27, 11(7):e0159972.
858 https://doi.org/10.1371/journal.pone.0159972

859 Boulet, R., Humbel, F.-X., Lucas, Y., 1982. Analyse
860 structurale et cartographie en pédologie. I- Prise en
861 compte de l'organisation bidimensionnelle de la
862 couverture pédologique : les études de toposéquences et
863 leurs principaux apports à la connaissance des sols. Cah.
864 ORSTOM, sér. Pédol. XIX, 309-321. Available from:
865 https://www.documentation.ird.fr/hor/fdi:03252

866 Cornell, R. M., Schwertmann, U. 2000. Iron Oxides in the
867 Laboratory: Preparation and Characterization. 2ed Ext.
868 WILEY-VCH. Weinheim.

869 Costa, M.P.F., Telmer, K.H., Evans, T.L., Almeida, T.I.R.,
870 Diakun, M.T., 2015. The lakes of the Pantanal: inventory,
871 distribution, geochemistry, and surrounding landscape.

Wetlands Ecology and Management, 23: 19-39. https://doi.org/10.1007/s11273-014-9401-3

Cotta, S.R., Pellegrinetti, T.A., Andreote, A.P.D., Costa, J.S., Sarmento, H., Fiore, M.F., 2022. Disentangling the lifestyle of bacterial communities in tropical soda lakes. Scientific Reports, v. 12, art. 7939. https://doi.org/10.1038/s41598-022-12046-2

Cudennec, Y. C., Lecerf, A. 2006. The transformation of ferrihydrite into goethite or hematite, revisited. Journal of Solid State Chemistry 179 (2006) 716–722. https://doi.org/10.1016/j.jssc.2005.11.030

Cunha, N.G. 1980. Considerações sobre os solos da sub-região da Nhecolândia, Pantanal Mato-Grossense. Corumbá, EMBRAPA-EUPAE de Corumbá, Circular técnico, 1. Available from: https://www.infoteca.cnptia.embrapa.br/handle/doc/787697

Curti-Martins, E.R.. 2012. Tipologia de Lagoas Salinas no Pantanal da Nhecolândia (MS). Thesis. Universidade de São Paulo, São Paulo. Available from:

https://www.teses.usp.br/teses/disponiveis/8/8135/tde-14012013-172446/pt-br.php

Ekosse, G.I.E. 2005. Fourier Transform Infrared Spectrophotometry and X-ray powder Diffractometry as Complementary Techniques in characterizing Clay size fraction of Kaolin. J. Appl. Sci. Environ. Mgt. Vol. 9 (2) 43-48. https://doi.org/10.4314/jasem.v9i2.17289

EMBRAPA, 2017. Manual de Métodos de Análise de Solo. (3ed ampl). Brasília. Available from: https://www.embrapa.br/busca-de-publicacoes/-/publicacao/1085209/manual-de-metodos-de-analise-de-solo

Freitas, J.G., Furquim, S.A.C., Aravena, R., Cardoso, E.L., 2019. Interaction between lakes' surface water and groundwater in the Pantanal wetland, Brazil. Env. Earth Sci. 78, 139. https://doi.org/10.1007/s12665-019-8140-4

Furian, S., Curti-Martins, E.R., Parizotto, T.M., Rezende-Filho A.T., Victoria, R.L., Barbiero, L., 2013. Chemical diversity and spatial variability in myriad lakes in Nhecolândia in the Pantanal wetlands of Brazil. Limnology

and Oceanography, 58: 2249-2261. Available from: https://hal.archives-ouvertes.fr/hal-02043233

Furquim, S.A.C., Graham, R.C., Barbiero, L., Queiroz-Neto, J.P., Vallès, V., 2008. Mineralogy and genesis of smectites in an alkaline-saline environment of Pantanal wetland, Brazil. Clays and Clay Minerals 56, 579- 595. https://doi.org/10.1346/CCMN.2008.0560511

Furquim, S.A.C., Graham, R.C., Barbiero, L., Queiroz-Neto, J.P., Vidal-Torrado, P., 2010a. Soil mineral genesis and distribution in a saline lake landscape of the Pantanal wetland, Brazil. Geoderma, 154, 518-528. https://doi.org/10.1016/j.geoderma.2009.03.014

Furquim, S.A.C., Barbiero, L., Graham, R.C., Queiroz-Neto, J.P., Ferreira, R.P.D., Furian, S., 2010b. Neoformation of micas in soils surrounding an alkaline-saline lake of Pantanal wetland, Brazil. Geoderma, 158, 331-342. https://doi.org/10.1016/j.geoderma.2010.05.015

Guerreiro, R. L. 2016. Mudanças paleoambientais no holoceno em lagoas salinas do Pantanal da Nhecolândia. Thesis. Universidade Estadual Paulista, Rio Claro.

Available from:
https://repositorio.unesp.br/handle/11449/147123

Guerreiro, R.L., Bergier, I., McGlue, M.M., Warren, L.V., Abreu, U.G.P., Abrahão, J., Assine, M.L., 2019. The soda lakes of Nhecolandia: a conservation opportunity for the Pantanal wetlands. Perspect. Ecol. Conserv. 17 (1), 9–18. https://doi.org/10.1016/j.pecon.2018.11.002.

GOOGLE. 2020. Google Earth Engine API. Avaiable from https://developers.google.com/earth-engine. Acessed at June 2nd, 2020.

Hamilton, S.K., Souza, O.C., Coutinho, M.E., 1998. Dynamics of floodplain inundation in the alluvial fan of the Taquari River (Pantanal, Brazil). SIL Proc. 1922–2010 (26), 916–922. https://doi.org/10.1080/03680770.1995.11900852

House, W. A., Orr, D.R., 1992. Investigation of the pH dependence of the kinetics of quartz dissolution at 25 C. Journal of the Chemical Society, Faraday Transactions, vol. 88, no 2, p. 233-241. https://doi.org/10.1039/FT9928800233

952 Icenhower, J. P., Dove, P. M., 2000. The dissolution kinetics
953 of amorphous silica into sodium chloride solutions: effects
954 of temperature and ionic strength. Geochimica et
955 Cosmochimica Acta, 64(24), 4193-4203.
956 https://doi.org/10.1016/S0016-7037(00)00487-7

957 INSTITUTO NACIONAL DE METEOROLOGIA - INMET.
958 Banco de Dados Meteorológicos para Ensino e Pesquisa
959 - BDMEP. Brasília, DF, Brasil, c2020. Disponível em:
960 http://www.inmet.gov.br/portal/index.php?r=bdmep/bdmep
961 . (accessed at 9 march 2020).

962 Ishida, D.A., Montes, C.R., Lucas, Y., Pereira, O.J.R.,
963 Merdy, P., Melfi, A.J. 2014. Genetic relationships between
964 ferralsols, podzols and white kaolin in Amazonia. Eur. J.
965 of Soil Sci, 65, 706–717.
966 https://doi.org/10.1111/ejss.12167

967 Jackson, M.L. 1985. Soil chemical analysis advanced
968 course, 5th print. Department of Soil Science University,
969 Wisconsin, Madison WI, 894p

970 Ji, J., Ge, Y., Balsam, W., Damuth, J.E., Chen, J., 2009.
971 Rapid identification of dolomite using a Fourier Transform

Infrared Spectrophotometer (FTIR): A fast method for identifying Heinrich events in IODP Site U1308. Marien Geology. 258, 60-68. https://doi.org/10.1016/j.margeo.2008.11.007

Jolliffe, I.T. 2002 Principal component analysis. 2nd ed, Springer-Verlag, New York

Kosmas, C. S, Curi, N., Bryant, R.B., Franzmeier, D.P., 1984. Characterization of iron oxide minerals by second derivative visible spectroscopy. Soil Science Society of America Journal, v. 48, n. 2, p. 401-405. https://doi.org/10.2136/sssaj1984.03615995004800020036x

Lainé, M., Balan, E., Allard, T., Paineau, E., Jeunesse, P., Mostafavi, M., Robert, J.-L, Le Caër, S., 2017. Reaction mechanisms in swelling clays under ionizing radiation: influence of the water amount and of the nature of the clay mineral. RSC Advances, 7 (256), 526-534. https://doi.org/10.1039/C6RA24861F

Li, X., Chang, S. X., Salifu, K. F. 2014. Soil texture and layering effects on water and salt dynamics in the

presence of a water table: a review. Environmental reviews, 22(1), 41-50. https://doi.org/10.1139/er-2013-0035

Macías, F., Camps-Arbestain, M. 2020. A biogeochemical view of the world reference base soil classification system: Homage to Ward Chesworth. Advances in Agronomy, Volume 160. https://doi.org/10.1016/bs.agron.2019.11.002

Mariot, M., Dudak, Y., Furian, S., Sakamoto, A., Vallès, V., Fort, M., Barbiero, L., 2007. Dissolved organic matter fluorescence as a water flow tracer in the tropical wetland of Pantanal of Nhecolândia, Brazil. Science of the Total Environment. 388, 183–196. https://doi.org/10.1016/j.scitotenv.2007.08.003

Malengrau, N., Bedidi, A., Muller, J.-P., Herbillon, A.J., 1996. Spectroscopic control of iron oxide dissolution in two ferralitic soils. European Journal of Soil Science, v. 47, p.13-20. https://doi.org/10.1111/j.1365-2389.1996.tb01367.x

1011 Merdy, P., Gamrani, M., Montes, C.R., Rezende-Filho, A.T.,
1012 Barbiero, L., Ishida, D.A., Silva, A.R.C., Melfi, A.J., Lucas,
1013 Y., 2022. Processes and rates of formation defined by
1014 modelling in alkaline to acidic soil systems in Brazilian
1015 Pantanal wetland. Catena, 210, 105876.
1016 https://doi.org/10.1016/j.catena.2021.105876

1017 Munsell Color (Firm). 1954. Munsell soil color charts.
1018 Baltimore.

1019 Nash, D.J., Ullyott, J.S., 2007. Silcrete. In: Geochemical
1020 Sediments and Landscapes, Nash, D.J., McLaren, S.J.
1021 (eds.). Oxford, UK, Blackwell Publishing, p. 95–148.
1022 https://doi.org/10.1002/9780470712917

1023 Oliveira Júnior, J.C., Andrade, G.R.P., Barbiero, L., Furquim,
1024 S.A.C., Vidal-Torrado, P., 2020. Flooding effect on
1025 mineralogical and geochemical changes in alkaline-sodic
1026 soil system of northern Pantanal wetlands. Brazil. Eur. J.
1027 Soil Sci. 71 (3), 433–447.
1028 https://doi.org/10.1111/ejss.12871

Pansu, M., Gautheyrou, J., 2006. Particle size analysis. In: Handbook of Soil Analysis. Springer, Berlin, Heidelberg, pp. 15–63. https://doi.org/10.1007/978-3-540-31211-6_2

Pellegrinetti, T.A., Cotta. S.R., Sarmento, H., Costa, J.S., Delbaje, E., Montes, C.R., Camargo, P.B., Barbiero, L., Rezende-Filho, A.T., Fiore, M.F., 2022. Bacterial Communities Along Environmental Gradients in Tropical Soda Lakes. Microbial Ecology. https://doi.org/10.1007/s00248-022-02086-6.

Pereira, O.J.R., Merino, E.R., Montes, C.R., Barbiero, L., Rezende-Filho, A.T., Lucas, Y., Melfi, A.J., 2020. Estimating water pH using cloud-based landsat images for a new classification of the Nhecolândia Lakes (Brazilian Pantanal). Remote Sens. 12, 1090. https://doi.org/10.3390/rs12071090

PLANET LABS. 2016. Planet Imagery Product Specification. São Francisco: Planet Labs, v. 56.

Russell, J.D. and Fraser, A.R., 1994. Infrared Methods. In: Wilson, M.J., Ed., Clay Mineralogy: Spectroscopic and Chemical Determinative Methods, Chapman and Hall,

London, 11-67. http://dx.doi.org/10.1007/978-94-011-0727-3_2.

Saikia, B.J., Parthasarathy, G., Sarmah, N.C., 2008. Fourier transform infrared spectroscopic estimation of crystallinity in SiO2 based rocks. Bull. Mater. Sci., Vol. 31, No. 5, 775–779. https://doi.org/10.1007/s12034-008-0123-0

Sakamoto, A.Y., Sakamoto, L.L.S., Neto, J.P.Q., Barbiero, L., 2004. Abordagem metodológica para o estudo de lagoas e Salinas do Pantanal da Nhecolândia, MS: fazenda São Miguel do Firme. IV Simp. Sobre Rec. Nat. e sócio-econômicos do Pantanal. Corumbá. Available from: https://docplayer.com.br/87510495-Abordagem-metodologica-para-o-estudo-de-lagoas-e-salinas-do-pantanal-da-nhecolandia-ms-fazenda-sao-miguel-do-firme.html

Salis, S.M., Lehn, C.R., Mattos, P.P., Bergier, I., Crispim, S.M.A., 2014. Root behavior of savanna species in Brazil's Pantanal wetland. Glob. Ecol. Conserv. 2, 378–384. https://doi.org/10.1016/j.gecco.2014.10.009.

1068 Scheinost, A.C., Chavernas, A., Barrón, V., Torrent, T.,
1069 1998. Use and limitations of second-derivative diffuse
1070 reflectance spectroscopy in the visible to near-infrared
1071 range to identify and quantify Fe oxide minerals in soils.
1072 Clays and Clay Minerals, v. 46, n. 5, p. 528-536.
1073 https://doi.org/10.1346/CCMN.1998.0460506

1074 Schwertmann, U., Friedl, J., Stanjek, H., 1999. From Fe(III)
1075 Ions to Ferrihydrite and then to Hematite. Colloid Interface
1076 Sci. 209, 215. https://doi.org/10.1006/jcis.1998.5899

1077 Souza Oliveira, N., Schiavo, J.A., Souza, A.C., Laranjeira,
1078 L.T., Moraes, E.M.V., Pereira, M.G., 2021. Mineralogy
1079 and genesis in an alkaline soil system in the southern
1080 Pantanal wetland, Brazil. South American Earth Sci. J.
1081 Volume 111, 103456.
1082 https://doi.org/10.1016/j.jsames.2021.103456

1083 Taylor, G., Eggleton, R.A., 2017. Silcrete: an Australian
1084 perspective. Australian Journal of Earth Sciences, 64(8),
1085 987-1016.
1086 https://doi.org/10.1080/08120099.2017.1318167

1087 Theodosoglou, E., et al., 2010. Comparative fourier
1088 transform infrared and x-ray powder diffraction analysis
1089 of naturally occurred k-feldspars. Bulletin of the
1090 Geological Society of Greece, XLIII, No.5, 2752.
1091 https://doi.org/10.12681/bgsg.11681

1092 USDA. United States Department of Agriculture. 1987. Soil
1093 Mechanics Level 1, Module 3, USDA Soil Textural
1094 Classification Study Guide. USDA Soil Conservation
1095 Service, Washington DC.

1096 Wilson, M.J., 1987. X-ray powder diffraction methods, in:
1097 Wilson, M.J. (Ed.), A Handbook of Determinative Methods
1098 in Clay Mineralogy. Chapman and Hall, New York, pp.
1099 26–98.

1100 Vaculíková, L., Plevová, E. 2005. Identification of clay
1101 minerals and micas in sedimentary rocks. Acta Geodyn.
1102 Geomater., Vol.2, No.2 (138), 167-175. Available at:
1103 https://www.irsm.cas.cz/materialy/acta_content/2005_02/2
1104 0_Vaculikova.pdf

1105 Vidoca, T. T. 2020. Gênese de argilominerais em solos
1106 afetados por sais no entorno de lagoas salobras do

Pantanal da Nhecolândia. Dissertation. Universidade de São Paulo, São Paulo. https://doi.org/10.11606/D.8.2020.tde-23092020-171253

Zhang, Y. G., Ji, J., Balsam, W.L., Liu, L., Chen, J. 2007. High resolution hematite and goethite records from ODP 1143, South China Sea: Co-evolution of monsoonal precipitation and El Nino over the past 600,000 years. https://doi.org/10.1016/j.epsl.2007.09.022

Zhou, J., Lau, K.-M. 1998. Does a Monsoon Climate Exist over South America? Journal of Climate, 11: 1020-1040. https://doi.org/10.1175/1520-0442(1998)011<1020:DAMCEO>2.0.CO;2

Zviagina, B.B., Drits, V. A., Dorzhieva, O.V. 2020. Distinguishing Features and Identification Criteria for K-Dioctahedral 1M Micas (Illite-Aluminoceladonite and Illite-Glauconite-Celadonite Series) from Middle-Infrared Spectroscopy Data. Minerals, 10, 153; https://doi.org/10.3390/min10020153

FIGURE CAPTIONS

Fig. 1. Water dynamics - Main routes of water transfer in an alkaline lake according to the literature. (For colour the reader is referred to the web version of this article)

Table 1. Saline-alkaline lake data - Parameters used to select representative saline-alkaline lakes within the study site.

Fig. 2. Location of study - Sites in the Nhecolândia area of the Taquari megafan, Pantanal, Brazil. Saline-alkaline lakes (1, 4, 6, 7) (B: black, G: green; C: crystalline) and freshwater lakes (F). T1 to T7: toposequences associated to the studied lakes. Satellite view from Google Earth. (For colour the reader is referred to the web version of this article)

Fig. 3. Landscape units - Typical vegetation along a saline-alkaline lake slope. (For colour the reader is referred to the web version of this article).

Fig. 4. Flooding monitoring - Interannual variability of the water level in the lakes studied. Satellite views from PlanetScope. (For colour the reader is referred to the web version of this article).

Fig. 5. Topographic data - Altitude of ridges and lake levels measured on the same day. Letters refer to points situated on the satellite view. (For colour the reader is referred to the web version of this article).

Fig. 6. Apparent electrical conductivity mapping of soils – ECS values around each saline-alkaline lake selected, with the delimitation of different landscape unit areas and the positioning of all boreholes. (For colour the reader is referred to the web version of this article).

Fig. 7. Nomenclature of the horizons – Scheme of the different color values, matrix hues and textures found in the studied soils.

Fig. 8. T1 - Main characteristics of the 1-Black lake toposequence. (a) ECS profile; (b) soil horizons, water levels, fine fraction and ECW values; c) soil pH. (For colour the reader is referred to the web version of this article).

Fig. 9. T4 - Main characteristics of the 4-Green lake toposequence. (a) ECS profile; (b) soil horizons, water levels, fine fraction and ECW values; c) soil pH. (For

colour the reader is referred to the web version of this article).

Fig. 10. T6 - Main characteristics of the 6-Black lake toposequence. (a) ECS profile; (b) soil horizons, water levels, fine fraction and ECW values; c) soil pH. (For colour the reader is referred to the web version of this article).

Fig. 11. T7 - Main characteristics of the 7-Crystalline lake toposequence. (a) ECS profile; (b) soil horizons, water levels, fine fraction and ECW values; c) soil pH. (For colour the reader is referred to the web version of this article).

Fig. 12. Soil mineralogy - Main minerals along the sequences. Black points indicate the analyzed samples. Unless otherwise stated, the following minerals have been identified at each point: quartz, feldspars, micas, kaolinite, 2:1 expandable clay minerals, goethite, hematite, ferrihydrite. The figure therefore represents the absence of one or more of these minerals or the presence of

calcite. (For colour the reader is referred to the web version of this article).

Fig. 13. Statistical data - PCA correlation circle between variables. Percentage on each factorial axis gives the explained variance. LOI: loss on ignition.

SUPPLEMENTARY MATERIAL CAPTION

File Name:

Manuscript_ARCS_Fev_2023_Submission_Supplemental File

Caption: Positioning, particle size distribution and pH in water of all samples collected for this research.